The Design and Characterization in Amplitude and Phase of a Compact 8-Channel Loop-Back AWG Based Integrated Comb Processor

L. Roel van der Zon, Luis A. Bru, Pascual Muñoz, *Senior Member, IEEE*, and Daniel Pastor

Abstract— This paper presents the design and characterization of an 8-channel integrated comb source spectral processor based on an arrayed-waveguide grating in loop-back configuration, with a channel spacing of 100 GHz. The arrayed waveguide grating has an unconventional mounting, for improved aberration and sidelobes. The design of the arrayed-waveguide grating, following a mathematical modeling method, is covered. The method presented gives an accurate result with the need for little computational power and no need for specific software. The devices, fabricated in a silicon nitride platform, are characterized for their spectral responses. The spectral processor is also characterized for both its amplitude modulation as well as the phase modulation. The phase modulation is characterized using optical frequency domain interferometry.

Index Terms— Spectral processor, waveshaper, comb processor, microresonator frequency comb, AWG, silicon nitride, phase modulation, optical frequency domain interferometry.

I. INTRODUCTION

SINCE their discovery, optical microcombs have awoken many interests. The ability of generating optical microcombs in a nanophotonic resonator has broadened their reach significantly [1], [2]. Amongst the applications that benefit from the use of an optical microcomb are the use of them as a photonic clock, light generation for LIDAR applications [3], arbitrary waveform generation, where two optical microcombs provide a signal that when mixed results in a radio frequency (RF) signal [4]. The advantage of using photonics to generate an electric RF signal is the ultrahigh analog bandwidth that can be achieved. To realize integrated microcomb-based systems, optical interposers are crucial for connecting, operating, and processing optical signals [5].

This work presents the design of an integrated comb processor (ICP), the function of the ICP is to apply an arbitrary amplitude and phase modulation to each of the eight frequency bands of an optical microcomb. The ICP is partly shown in Fig. 1, as well as the design and simulation of a 9-channel
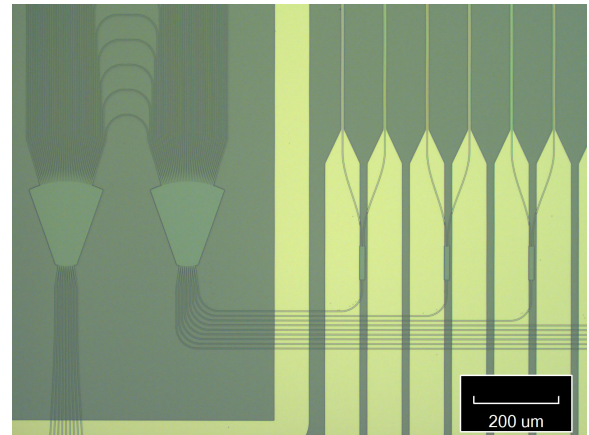
Fig. 1.　A microscope picture of a part of the manufactured ICP. The dark lines are structures in deep etched Si_3N_4, the light part is the metal layer.

arrayed-waveguide grating (AWG), used to construct the loop-back layout. The characterization of this complex device, in terms of its spectral response, amplitude modulation and phase modulation is shown.

There are several ways to design and simulate an AWG, where the most accurate tools usually simulate the field propagation through the free propagation region (FPR) of the star coupler and the fastest methods rely on design rules and mathematical approximations to define the dimensions and estimate the performance. Simulating the light propagation through the FPR is computationally heavy and done by specialized software. Depending on the tools at hand, the result is either a rough estimation or not obtainable without heavy computational force. The design strategy presented here adapts a mathematical strategy presented in [6], which consumes little computing power, but yields accurate results, using only few input characteristics such as the effective index and mode field diameter of the components used. A fast simulation enables the designer to create better performing devices, because the impact of design choices can be evaluated quickly.

The characterization of the ICP is split into two ways. First the spectral response of the AWG will be presented, followed by the amplitude modulation, both using standard measurements techniques, and have been presented in [7]. Then the characterization of the phase modulation, which has been presented in [8], covers the last part.

The characterization of the phase response of a device is not straightforward, and it can be made by employing different

interferometric techniques. When accessing the integrated device using optical fibers, their sensibility against environmental conditions provokes a direct estimation of phase to result in poor reproducibility, preventing comparison between direct phase estimations of consecutive measurement takes. However, phase assessment referenced to a strategic local contribution eliminates that source of instability, and enables estimation of phase evolution as demonstrated by employing Optical Frequency Domain Interferometry (OFDI) [9]. OFDI is a swept-wavelength technique that allows for the characterization of photonic devices with high resolution [10], [11], which makes it suitable for integrated devices. The optical amplitude and phase response of the device under test (DUT) can be assessed in both the time and the spectral domains. The referenced optical phase assessment can be performed by comparing contributions in the time domain [12]. Here, similarly to [13], we retrieve the phase characteristics of the ICP in the frequency domain by adapting the technique as detailed in the corresponding section below.

II. Design and Fabrication

A. Fabrication Platform

The devices were fabricated at Myfab Chalmers [14]. The comb processor is designed in a Si_3N_4 platform with SiO_2 substrate and cladding. The substrate is thermally oxidized silicon. The thermal oxide thickness is $3\,\mu m$ with a refractive index of 1.4431 at 1550 nm, the LPCVD Si_3N_4 is 200 nm thick and has a refractive index of 1.99. The top cladding is fabricated as first a layer of $1\,\mu m$ of LPCVD SiO_2 with a refractive index of 1.4439. On top is a $2\,\mu m$ of PECVD SiO_2 with refractive index 1.4595. The structures are defined via electron-beam lithography using a $500\,\mu m$ square writing field and are deep etched. The fabrication of the Si_3N_4 structures follows the procedure described in [15]. A picture of the manufactured ICP is shown in Fig. 1.

B. AWG Design

The chip has been fabricated using different dimensions than the usual waveguides as fabricated by Myfab. The cross section of the deep etched waveguides measures $1.35\,\mu m$ wide and $0.2\,\mu m$ high. The bend radius for all bends is chosen at $50\,\mu m$, to keep the bend losses low. To estimate the effective indices, cross section simulations have been performed using Synopsis OptoDesigner. From simulation the following effective indices, for the central wavelength of 1550 nm, are found: 1.4999 for straight waveguide, 1.5017 for the bends and 1.5733 for the FPR. The waveguides support TE, single mode, only. For approximation of the mode profile at the end of the $3\,\mu m$ wide in- and output tapers, a Gaussian distribution is fitted to the simulated mode. The radius of the Gaussian approximation is $1.3\,\mu m$

To design and simulate the AWG, a mathematical model was made. First the dimensions of the star couplers and array waveguides are decided, then a simulation is performed. The star coupler is defined using Rowland circle geometry, where the inputs are located along a radius half the radius used for the placement of the array waveguides. The array waveguides
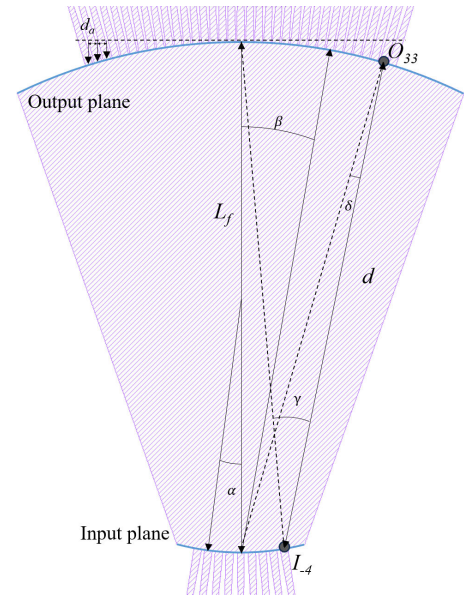

Fig. 2. The 9 by 35 star coupler with focal length L_f. The design angles α and β indicate the locations of the in- and outputs and are defined during the design phase. The in- and output planes of the star coupler and the angles γ and δ are used to calculate the field projections, in this case from I_{-4} and O_{33}. The distance d is used to calculate the phase contribution of the FPR. The unconventional mounting, according to [16], is indicated, where d_a is the array waveguide spacing.

are placed in an unconventional way, the array waveguides are spaced equidistant on a line tangent to the radius of the star coupler, as shown in Fig. 2. Unlike the conventional way where a constant pitch is used to place the star coupler outputs. This greatly improves the sidelobe suppression and gives a decrease in aberration [16]. There are 35 array waveguides, which are spaced at $3.5\,\mu m$ on the tangent line, to leave at least $0.5\,\mu m$ of gap between them, required for fabrication. The in- and output waveguides are tapered from 3 to $1.35\,\mu m$. Their length has been defined using geometrics, taking into account the length and effective index of each section, the total length of the array waveguides can be chosen, such that in each subsequent waveguide exactly m more wavelengths, at the central wavelength, $\lambda_0 = 1550$ nm, fit in the array waveguide. The AWG design variable m defines the free spectral range (FSR) in frequency of the AWG [6]:

$$FSR = c_0/(m * \lambda_0) \tag{1}$$

where c_0 is the speed of light.

The layout is chosen as orthogonal, where the array waveguides are composed of a taper, a bend to the normal, and 3 straight sections connected with two 90 degree bends, and a bend to the taper of the second slab. However, other layouts have been studied, such as a variable radius design, where the arrayed waveguides are constructed of two straight sections and only one bend, with a radius specific for the design length, as well as a design with only two bends of equal radius and 3 straight sections of waveguide. The orthogonal layout was the most efficient in floorspace, caused the least amount of stitches between writing fields and was less restricting in design parameters. Stitches between writing fields are assumed
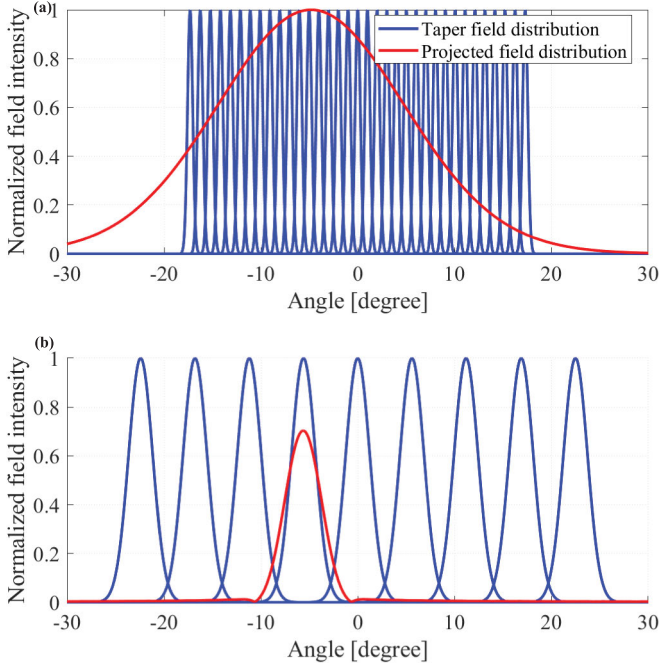
Fig. 3. The field distributions in the star couplers, for $\lambda = 1547.61$ nm. The field distributions are approximated as a Gaussian. The taper field distributions are displayed in blue and their radius is based on the Gaussian fit on the mode profile. The projected distributions, in red, are calculated by (3) for only one input in the first star coupler (a) and as a sum of distributions for the second star coupler (b). The angles represent the location along the respective in- and output plane of the star coupler. Note that the incoming beam (red) in the first star coupler (a) is off center, due to an error in the floor plan.

to result in losses as well as small perturbations in length, which can cause phase errors.

Then a simulation is performed. The first star coupler is modeled using Gaussian approximations of the fields. The field shape at each input waveguide on the first slab coupler is:

$$f(x) = e^{-(\frac{x}{\omega_0})^2} \quad (2)$$

where ω_0 is the mode field radius. The input is then translated, using Fourier optics, to the far field illuminating the output radius of the star coupler:

$$F(-s) = \int_{-\infty}^{\infty} f(x)e^{j2\pi sx} \, dx \quad (3)$$

where:

$$s = n_{FPR}sin(\gamma)/\lambda \quad (4)$$

where n_{FPR} is the effective index in the FPR, γ is the angle between the normal of the input taper and the location on the output radius of the star coupler and λ the wavelength simulated. The field shape of the tapers at the FPR output feeding the array waveguides is also represented by a Gaussian profile, by translating (2) to the corresponding angles:

$$f_{taper}(\gamma) = e^{-(L_f sin(\gamma + \beta_i)/w_0)^2} \quad (5)$$

where β_i is the placement angle of the star coupler's output port and γ the angles along the output plane of the star coupler. The resulting field distributions are presented in Fig. 3.

The phase contribution from the light travelling through the star coupler is calculated along the output plane of the star coupler. It is important to take the phase contribution into account,

because the phase of the projected field is not constant along the width of the tapers, resulting in a slightly reduced coupling efficiency. The coupling efficiency to the array waveguides is estimated by an overlapping integral between both field distributions:

$$\eta = \frac{\left| \int F_{in}^* f_{taper} \, d\gamma \right|^2}{\int |F_{in}|^2 d\gamma \, \int |f_{taper}|^2 d\gamma} \quad (6)$$

where F_{in} is the projected field, along the output plane of the star coupler, coming from (3) and (4).

The phase contribution in the array waveguides is estimated taking into account the distance traveled and effective index for each part, and each wavelength. The phase contributions for the tapers have been neglected since each array waveguide has the same taper, contributing equally. The array waveguides have been assumed lossless.

To estimate the coupling efficiency in the second star coupler a similar approach is followed. However, now we are dealing with multiple inputs that project a field on the input plane of the star coupler. To resemble this projection a sum of all incoming beams has to be taken.

$$f(\delta) = \sum_{i=1}^{n} F(\delta) \cdot \phi(\delta) \cdot E_{in_i} \quad (7)$$

where $F(\delta)$ represents the far field from the wave broadening in the FPR, derived from (3), $\phi(\delta)$ is the phase contribution from the input taper to a location, defined by angle δ on the input plane of the star coupler, E_{in} the inputs of all array waveguides as a complex number, containing both amplitude and phase and n the number of array waveguides. The resulting field distribution for the central wavelength is shown in red Fig. 3 (a). The coupling is again estimated by an overlapping integral of both fields. This time the resulting coupling efficiency is multiplied the total estimated power that entered the array waveguides.

To verify the accuracy of the model, for the first slab coupler, a BPM simulation is performed in Synopsys Optodesigner. The resulting coupling efficiency is showed together with the result from the Gaussian approximation above in Fig. 4. The Gaussian approximation gives a total coupling efficiency of 0.71, where the BPM result estimates 0.69.

The AWG in- and outputs, which taper to 3 μm, are placed at locations defined by the simulation result. By running a quick and simplified simulation, neglecting accurate coupling efficiency, the correct location, where the field intensity is highest for the given wavelength, can be chosen.

The full response, as simulated, is shown in Fig. 5 (a). According to the simulation the designed 9-channel AWG should give a 27 dB suppression of the neighboring channel, at its center. The losses are estimated to range from 2 dB, for the left channel to 4.7 dB, for right channel, when using the right channel as an input.

In designing the AWG a performance limiting error was made. The star coupler input waveguides face the center of their Rowland circle, instead of the center of the opposed output radius. This results in more coupling losses, the simulations represent this error. A correct placement would result
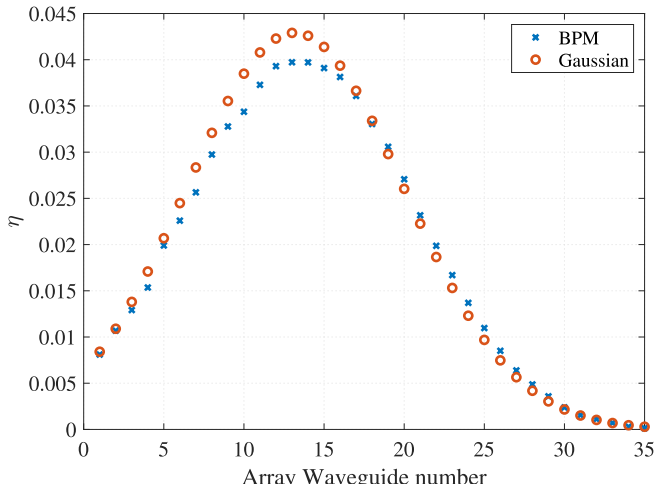
Fig. 4. The comparison of the coupling efficiency as estimated by the presented Gaussian aproximation and a BPM simulation performed in Synopsys Optodesigner. The total coupling efficiency of the star coupler is estimated to be 0.71 in case of the Gaussian Approximation and 0.69 for the BPM simulation.
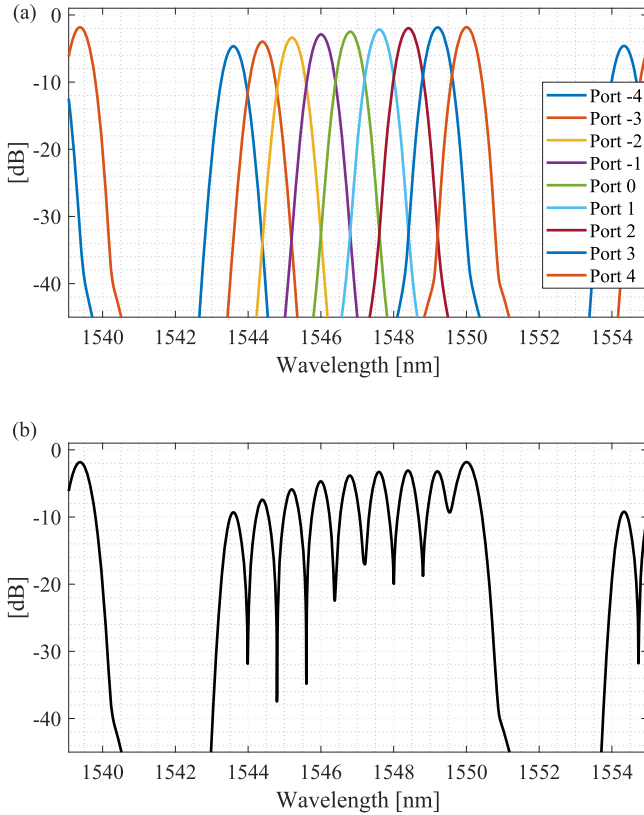

Fig. 5. The simulated spectral response of the AWG (a), which gives 2-4.7 dB of insertion losses, and the simulated result of the loop-back layout used for the ICP (b), which results in 3.2-9.3 dB of insertion loss.

in a more uniform spectral response and in about 2.3 dB less losses.

C. ICP Layout

For the ICP layout a loop-back configuration has been chosen for the benefits it gives: Only one AWG is used for both DEMUX as well as MUX. This avoids the matching problems and reduces floorspace. The downside is that the input of the
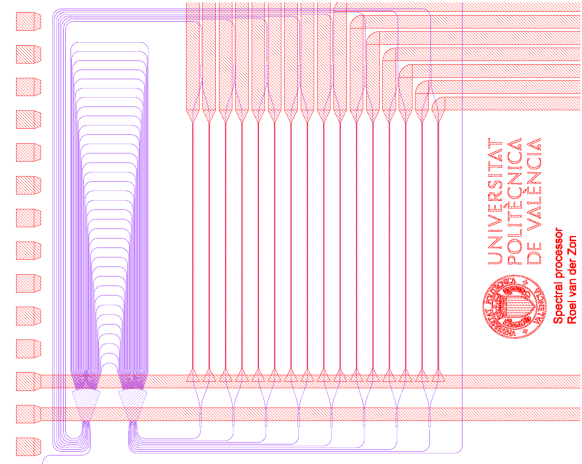

Fig. 6. The floorplan of the spectral processor. The structures in Si_3N_4 are displayed in purple, the metal layer in red. The total device measures 2.4 mm by 2.7 mm.

ICP intrinsically has one AWG channel of which there is no control over and which channel output will be more powerful than that of the the controllable channels.

By running the same AWG simulation again, but this time taking the output of the AWG as the input, the output of the ICP is obtained. The simulated ICP spectral response is shown in Fig. 5 (b). Both the signal resulting from the loop-back, recombining at the left hand side, as well as the original input at the right are visible. The ICP channel show a loss of 3.2 to 9.3 dB, which is about double the AWG's insertion loss. It is estimated that the ICP channels can be suppressed with 28 dB, but to achieve such performance the MZIs need to reach at least 30 dB of suppression.

To modulate the ICP channels the arms of the loop-back are equipped with balanced Mach Zehnder Interferometers (MZI) which have 1.5 mm long and 5 μm wide platinum thermal tuners in both paths. The resistance of the tuners is 215 Ω The floorplan of the ICP is shown in Fig. 6.

The device is accessed using grating couplers. The grating couplers consist of a 17.55 μm wide grating with grating period 1.17 μm having 11 fully etched grating periods. They are connected to standard waveguides on the processor through 200 μm tapers. The spectral response of a straigth waveguide connected trought two grating couplers is shown in Fig. 7. This trace has been used to normalize the spectral responses of the other measurements. From one grating coupler to another the response differed slightly, the measurements were also sensitive for correct alignment, where a slight offset in alignment did affect the coupling efficiency and the flatness of the response. The injection loss from grating coupler to grating coupler was at least 24 dB, which is relatively high. This however did not affect the characterization of the ICP.

III. CHARACTERIZATION

A. Spectral Response and Amplitude Modulation

The spectral response and amplitude modulation has been characterized using a broadband source (NP Photonics ASE-CL-20-S) and Optical Spectrum analyzer (OSA) (Yokogawa AQ6370C). The AWG response coming from the
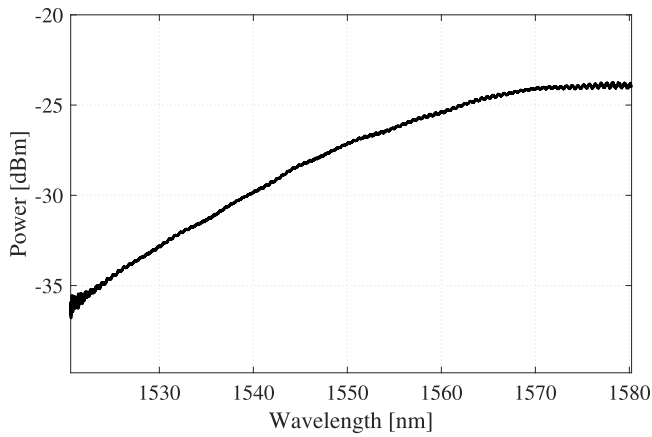
Fig. 7. The spectral response of a straight waveguide connected through grating couplers.
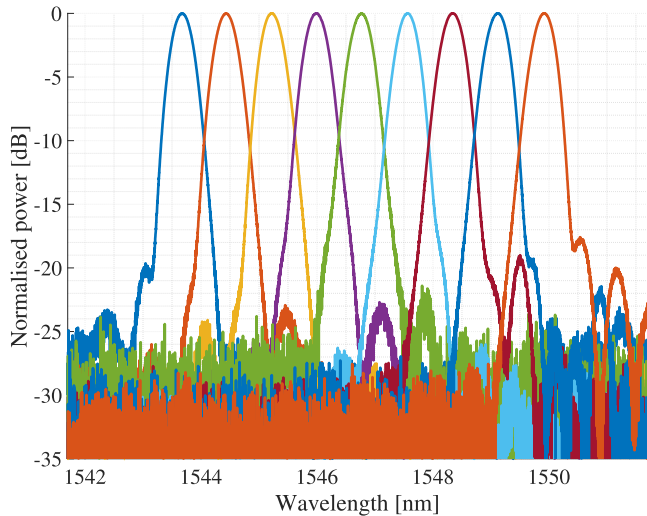

Fig. 8. Spectral response of the AWG. The 9 channels have been measured separately through grating couplers and their responses have been normalized to overcome the differences in coupling efficiency.
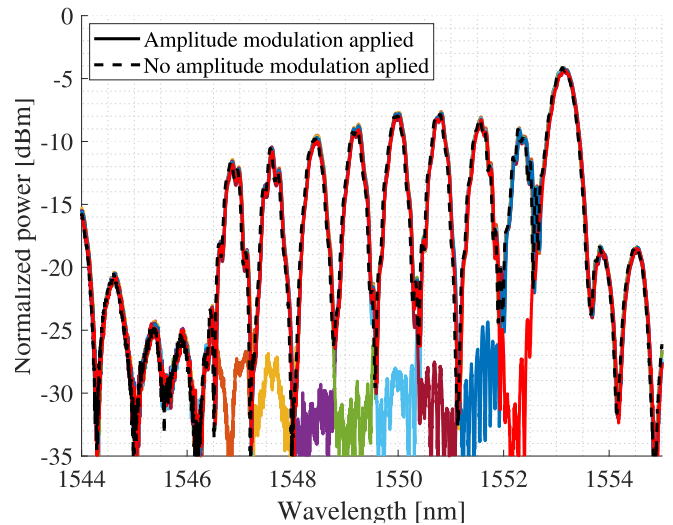

Fig. 9. Spectral processor transmission with the dashed line when no amplitude modulation is applied and the colored lines for each channel when the amplitude is lowered to its minimum, resulting in about 22 dB suppression of the channels. The graph also shows that there is no visible crosstalk between the MZIs.
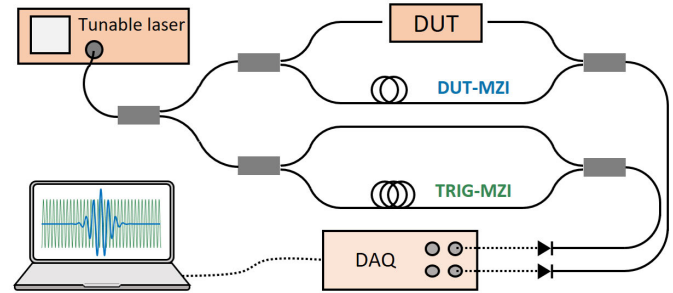

Fig. 10. OFDI setup sketch: The TL is connected to two interferometers: the DUT-MZI, with a given PLD, includes the DUT. After TL sweep, the resulting interferogram is photodetected, captured by a DAQ, and data stored to be processed. The TRIG-MZI, with a higher PLD, is used for linearization of the DUT interferogram.

fabricated device is shown in Fig. 8. Here the AWG channels have been measured seperately, due to a varying coupling efficiency it was chosen to normalize all channels to 0 dB. Only in some channels the first sidelobe is visible, in others it is out of the measurable range of the equipment. The suppression of neighboring channels, at the center of each channel is more than 25 dB, but at the limit of the OSA's sensitivity level.

The amplitude modulation is characterized by applying a current between 32 and 37 mA to one of the heaters of the MZI to suppress the signal in the selected ICP channel. A spectral response showing both the suppressed as well as unsuppressed channels is shown in Fig. 9. The spectral response shows that the channels can be suppressed up to 22 dB. To characterize the thermal crosstalk in the amplitude modulation a separate measurements with a fixed wavelength laser was performed. The experiment was done for both the MZIs in the ICP loop-back, as well as a set of separate MZIs. In the case for the MZIs in the ICP loop-back 0.8% of crosstalk was measured. The seperate MZIs showed no measurable crosstalk. The crosstalk in the ICP can likely be caused by a shift of the central wavelength of the ICPs AWG, due to a change in temperature of the chip. Lastly, a 90% drop as well as a 90% rise in optical throughput is achieved in less than 35 μs, which corresponds to literature for similar tuners [17]. The suppression reached in the separate MZIs was 37 dB.

B. Phase Response

1) Experiment: The phase response of the ICP channels is controlled by sending an equal current through both heaters of a MZI. An equal phase shift results in unchanged recombination at the end of the MZI, but alters the phase of the ICP channel. A π phase shift requires a 37 mA current through the 215 Ω heaters, so that a 588 mW power consumption is needed to realize a π phase shift with both MZI heaters.

The ICP shows very low crosstalk in terms of amplitude modulation. However crosstalk, or other forms of disturbance, were observed in the phase response of the device. This effect may be due to temperature changes and to the different length of the loop-back arms. Therefore, during the characterization of the ICP phase modulation, the device has been mounted on a chuck whose temperature is maintained stable, at room temperature, using a Peltier element and a temperature controller.
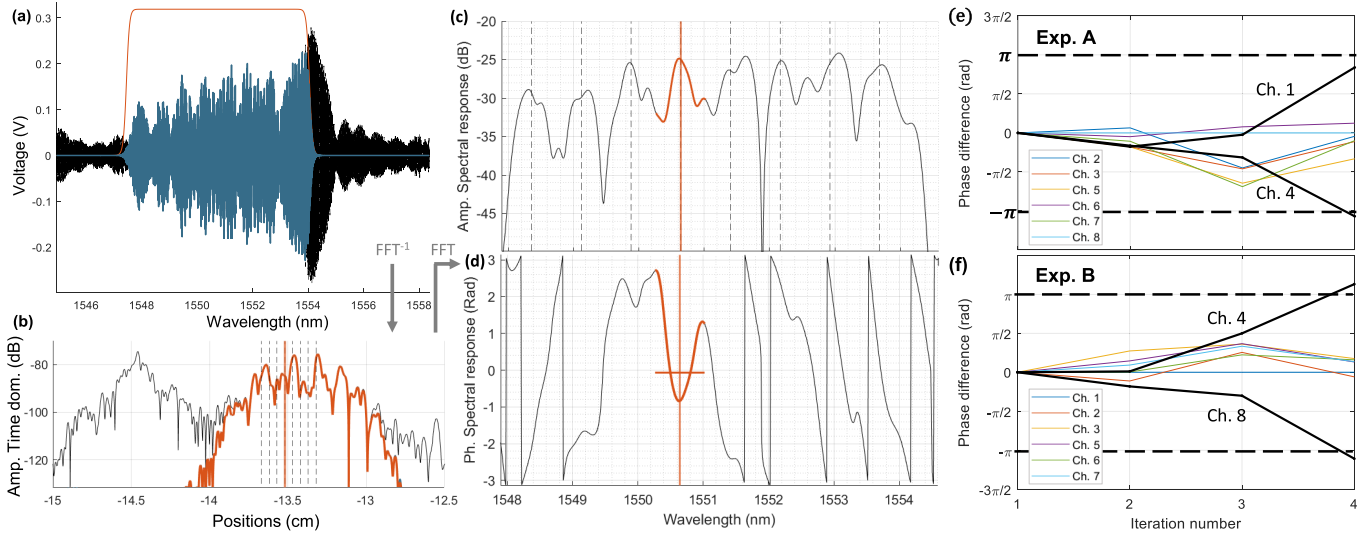
Fig. 11. (a-d) OFDI processing including DUT interferogram (a), time domain response (b), and amplitude (c) and phase spectral response (c) reconstructed from individual channel re-centering process. (b) Phase differences (e),(f) for the two performed experiments.

Besides, the experiments were executed in such a way that the total power dissipated on the chip is maintained equal. In other words, when rising the current through one heater, the current through another is reduced. The chip has been wirebonded to a PCB to access the electrical connections, and two experiments have been carried out, namely A and B. The phase modulation is performed on channels 1 and 4, and 4 and 8, for A and B, respectively.

As shown in Fig. 10, in the OFDI setup DUT is accessed through one of the arms of the DUT-MZI, with a given path length difference (PLD). A tunable laser (TL) wavelength sweep of 100 nm span around $\lambda = 1550$ nm is performed, giving an interference pattern that is photodetected and transformed to digital data employing a digital acquisition card (DAQ). The resulting DUT interferogram is properly linearized in frequency by using a secondary interferogram, generated by the TRIG-MZI with higher PLD, a common procedure in OFDI [9], [10], [11]. The linearized DUT interferogram can be processed to access the amplitude and phase time domain response of the DUT. The phase relation between different temporal features can be assessed in OFDI, so that its evolution can be analyzed from one measurement take to another [12]. Along with extra processing in the time domain that we propose in this paper, and describe below, it is possible to analyze the phase relations between different wavelength channels as well. This makes OFDI a suitable technique to characterize the phase response of the ICP.

2) Results: In Fig. 11 (a), the obtained interferogram for the first iteration of experiment A is shown. The interferogram is pass filtered to a single central band (shown in blue), where the ICP channels are found. Then, inverse fast Fourier transform (FFT) is applied to obtain the time domain response (b). The resulting trace in amplitude is shown, zoomed to the region of interest. The broadened peak at the left corresponds to the remaining direct AWG contribution, while the ICP channels contributions, each of them convolved with the AWG response correspondingly, are superimposed in the second (highlighted

in orange) group at the right, where their center positions are indicated with dashed lines. The next processing step consists of applying a window filter to isolate the ICP contributions, and then conduct a trace crop to re-center the trace, individually, to the positions of the channel centers. Under these conditions, ideally, the corresponding spectral phase response plateaus along the corresponding frequency region of the channel. Hence, we proceed accordingly and, once the re-centered traces are available for each of the 8 channels, FFT algorithm is systematically applied to reconstruct the corresponding spectra, obtaining amplitude and phase traces as shown in Fig. 11 (c) and (d) for channel 4. As expected, the phase curve, although somewhat affected by adjacent channels, is fairly steady in the region of the channel band. The spectral amplitude is also shown above, where just the 8 ICP channels are visible, having disappeared the direct AWG contribution after its complete removal in the time domain picture. Phase is then assessed in the region of the channel for each case. While these values lack of physical meaning separately, and vary from one measurement take to another in OFDI [9], a relative evaluation of them is done and, accordingly, we calculate the phase differences between each channel and the outer channel, i.e. channel 8 and 1 for experiments A and B, respectively. Since iteration 1 corresponds to the origin of heater tuning, we set this phase difference to zero, as reference, and compute the evolution of this quantity along the electrical tuning iterations. The results for both experiments are shown in Fig. 11 (e) and (f) where, as expected, the corresponding traces for the tuned channels (in bold grey and black curves) evolve from 0 to, roughly but clearly, $\pm\pi$, while the unperturbed channels (shown in different colors) maintain a steadier evolution, not exempt from a certain degree of variation, probably due to some temperature crosstalk on the chip during the experiments.

IV. CONCLUSION

A mathematical model to design and simulate an AWG is presented. It proved to give accurate results, with minimum computational power. Differences between the model and the

manufactured device could be attributed to manufacturing imperfections and variations in coupling efficiency between one grating coupler and another. Phase errors caused due to for example roughness, stitches or a variation in width or height of the waveguides can cause a phase error. These errors both influence the coupling efficiency as well as the rejection of wavelengths of other channels. The model is based on valid assumptions to simplify the physics, but to correctly validate the model more manufacturing results could be desired.

The spectral response of the ICP, presented in [7], resembles the simulation result of the model. The difference in range of amplitude modulation, which can be modulated gradually, can be attributed to the performance of the MZI and manufacturing errors. The insertion loss has not been characterized, due to the use of grating couplers which suffered a substantial variance in insertion loss. However, by looking at the amplitude difference between the controllable ICP channels and the uncontrollable channel, higher in amplitude, we can get a good estimate. Light present in the uncontrollable channel passes only once through the AWG, light in all other channels has to pass twice. The simulation result gives 1.4 to 7 dB of difference between the two, the measurement show a difference between 4 and 7 dB.

For the characterization of the phase response an OFDI technique as described in [9] has been adapted successfully. The experiments show that the device's phase modulation evolves along the tuning range. Hereby the experiments demonstrate a correct functioning of the device. However, some thermal crosstalk is present between the ICP channels loop-back arms. This crosstalk, together with channel crosstalk coming from the AWG results in some change in phase response of the unperturbed channels. Device performance may be improved by better isolating the ICP channels, both in terms of thermal crosstalk, as well as in optically isolating the channels in the AWG. Thermal crosstalk can be addressed adopting isolating techniques such as the implementations of air trenches along the heaters. The path lengths of the ICP loop-back channels can also be corrected to have the same length and therefore a temperature change affects the channels equally. The AWG performance can be improved by using more array waveguides and/or a longer FPR.

For future works it should be noted that when selecting an AWG channel which is not the center channel, the channel spacing alters slightly, about 0.01 nm in this example. For small AWGs this is not a problem, but is measurable. When designing the AWG using the center channel, the phase of the light entering the array waveguides is equal. For any other input channel the distance to the outgoing star coupler tapers is unequal and due to dispersion the AWG response will be slightly different. When designing a processor with a greater number of channels, the ICP channel spacing should correspond to the source channel spacing more closely, to have all channels correspond correctly to a comb line wavelength. It is recommended to adjust the placement simulations to represent the actually used channel as in- and output of the ICP.

The ICP could be used as an optical interposer and with that opens a viable path for on chip RF arbitrary waveform generation [4]. However, a common Si_3N_4 thickness for broadband comb sources is 790 nm [5], for comb generation and modulation on the same chip, this difference in thickness can be overcome with use of photonic interposers.

Although the thermo-optical phase modulators used, chosen for their robustness, provide rise times of the order of tens of microseconds (corresponding to actuation frequencies of the order of tens of kHz), due to the intrinsic limitations of thermal dynamics. Other actuation mechanisms, being reasonably compatible with Silicon Nitride technology, have been demonstrated such as Micro-electromechanical actuators [18] or actuators based on PZT materials [19] (even combined with thermo-optical elements [20]) that allow the actuation frequencies to be raised to hundreds of MHz.

REFERENCES

[1] S. T. Cundiff and J. Ye, "Colloquium: Femtosecond optical frequency combs," *Rev. Mod. Phys.*, vol. 75, pp. 325–342, Mar. 2003, doi: 10.1103/RevModPhys.75.325.

[2] A. L. Gaeta, M. Lipson, and T. J. Kippenberg, "Photonic-chip-based frequency combs," *Nature Photon.*, vol. 13, no. 3, pp. 158–169, Mar. 2019, doi: 10.1038/s41566-019-0358-x.

[3] A. Lukashchuk, J. Riemensberger, M. Karpov, J. Liu, and T. J. Kippenberg, "Dual chirped microcomb based parallel ranging at megapixel-line rates," *Nature Commun.*, vol. 13, no. 1, p. 3820, Jun. 2022, doi: 10.1038/s41467-022-30542-x.

[4] B. Wang, Z. Yang, S. Sun, and X. Yi, "Radio-frequency line-by-line Fourier synthesis based on optical soliton microcombs," *Photon. Res.*, vol. 10, no. 4, p. 932, Apr. 2022. [Online]. Available: https://opg.optica.org/prj/abstract.cfm?URI=prj-10-4-932

[5] A. Rao et al., "Towards integrated photonic interposers for processing octave-spanning microresonator frequency combs," *Light, Sci. Appl.*, vol. 10, no. 1, p. 109, May 2021, doi: 10.1038/s41377-021-00549-y.

[6] P. Munoz, D. Pastor, and J. Capmany, "Modeling and design of arrayed waveguide gratings," *J. Lightw. Technol.*, vol. 20, no. 4, pp. 661–674, Apr. 2002. [Online]. Available: http://jlt.osa.org/abstract.cfm?URI=jlt-20-4-661

[7] L. R. van der Zon, P. Muñoz, D. Pastor, M. Girardi, and V. Torres-Company, "Compact 8-channel loop-back AWG based integrated comb processor," in *Proc. IEEE 17th Int. Conf. Group IV Photon. (GFP)*, Dec. 2021, pp. 1–2. [Online]. Available: https://ieeexplore.ieee.org/document/9674008

[8] L. R. van der Zon, P. Munoz, D. Pastor, M. Girardi, and V. Torres-Company, "Compact 8-channel loop-back AWG based integrated comb processor," in *Proc. 24th Eur. Conf. Integr. Opt.*, Twente, The Netherlands, Apr. 2023, pp. 36–38. [Online]. Available: https://www.ecio-conference.org/wp-content/uploads/2023/05/VanderZon_Integrated_Comb_Processor.pdf

[9] L. A. Bru, "Optical frequency domain interferometry for the characterization and development of complex and tunable photonic integrated circuits," Ph.D. dissertation, Departamento de Comunicaciones, Universitat Politècnica de València, Valencia, Spain, 2022. [Online]. Available: http://hdl.handle.net/10251/181635

[10] U. Glombitza and E. Brinkmeyer, "Coherent frequency-domain reflectometry for characterization of single-mode integrated-optical waveguides," *J. Lightw. Technol.*, vol. 11, no. 8, pp. 1377–1384, Aug. 1993.

[11] B. J. Soller, D. K. Gifford, M. S. Wolfe, and M. E. Froggatt, "High resolution optical frequency domain reflectometry for characterization of components and assemblies," *Opt. Exp.*, vol. 13, no. 2, pp. 666–674, 2005. [Online]. Available: https://opg.optica.org/oe/abstract.cfm?URI=oe-13-2-666

[12] J. Fernandez, L. A. Bru, D. Pastor, D. Domenech, C. Domínguez, and P. Muñoz, "Sagnac reflector based broadband tunable integrated mirror," in *Proc. 22nd Int. Conf. Transparent Opt. Netw. (ICTON)*, Jul. 2020, pp. 1–5.

[13] K. Twayana, Z. Ye, Ó. B. Helgason, K. Vijayan, M. Karlsson, and V. Torres-Company, "Frequency-comb-calibrated swept-wavelength interferometry," *Opt. Exp.*, vol. 29, no. 15, pp. 24363–24372, Jul. 2021. [Online]. Available: https://opg.optica.org/oe/abstract.cfm?URI=oe-29-15-24363

[14] *Myfab Chalmers Nanofabrication Laboratory*. Accessed: Sep. 29, 2023. [Online]. Available: https://www.chalmers.se/en/infrastructure/myfab-chalmers/

[15] X. Hu, M. Girardi, Z. Ye, P. Muñoz, A. Larsson, and V. Torres-Company, "Si$_3$N$_4$ photonic integration platform at 1 *mu* for optical interconnects," *Opt. Exp.*, vol. 28, no. 9, pp. 13019–13031, Apr. 2020. [Online]. Available: http://www.opticsexpress.org/abstract.cfm?URI=oe-28-9-13019

[16] J. Zou, Z. Le, J. Hu, and J.-J. He, "Performance improvement for silicon-based arrayed waveguide grating router," *Opt. Exp.*, vol. 25, no. 9, p. 9963, May 2017. [Online]. Available: http://www.opticsexpress.org/abstract.cfm?URI=oe-25-9-9963

[17] R. Alemany, P. Muñoz, D. Pastor, and C. Domínguez, "Thermo-optic phase tuners analysis and design for process modules on a silicon nitride platform," *Photonics*, vol. 8, no. 11, p. 496, Nov. 2021. [Online]. Available: https://www.mdpi.com/2304-6732/8/11/496

[18] N. Quack et al., "Integrated silicon photonic MEMS," *Microsyst. Nanoeng.*, vol. 9, no. 1, p. 27, Mar. 2023.

[19] A. Bancora et al., "Frequency agile photonic integrated external cavity laser," in *Proc. CLEO*. San Jose, CA, USA: Optica Publishing Group, May 2023, Paper no. SF2Q.1. [Online]. Available: https://opg.optica.org/abstract.cfm?URI=CLEO_SI-2023-SF2Q.1

[20] H. Tian et al., "Programmable silicon nitride photonic integrated circuits," in *Proc. IEEE 36th Int. Conf. Micro Electro Mech. Syst. (MEMS)*, Jan. 2023, pp. 149–152.

Pascual Muñoz (Senior Member, IEEE) was born in Valencia, Spain, in February 1975. He received the Ingeniero de Telecomunicación degree and the Ph.D. degree in photonics from the Universitat Politècnica de València (UPV) in 1998 and 2003, respectively. In 1999, he was with 1st Lieutenant in the Spanish Airforce, while working as an IT Consultant with the AIME Instituto Tecnológico. He is currently a Full Professor with the Departamento de Comunicaciones and a Researcher with the Institute for Telecommunications and Multimedia Applications (ITEAM), UPV. He runs a consolidated research line, started in 2005, on prototyping photonic integrated circuits (PICs) in a technology agnostic fashion, where PICs are designed in the best suited technology (silicon-on-insulator, indium phosphide, silica on silicon, and silicon nitride) for each application. He has been involved in several European Commission funded projects, being a Coordinator for integration on InP within the NoE IST-EPIXNET. He has published over 50 papers in international refereed journals and over 80 conference contributions. He is a member of the Technical Programme Committees of European Conference on Optical Communications (ECOC) and European Conference on Integrated Optics (ECIO). He received the VPI Speed Up Photonics Award in 2002 for innovative Fourier optics AWG with multimode interference (MMI) couplers modeling, by Virtual Photonics Incorporated and *IEEE Communications Magazine*. He was also granted the IEEE/LEOS Graduate Student Fellowship Program in 2002. He received the Extraordinary Doctorate Prize from UPV in 2006. From his research line, he co-founded UPV spin-off company VLC Photonics in 2011, where the PIC design know-how, expertise and tools have been transferred. He was the CEO from 2011 to 2013. He is a Senior Member of the OSA.

L. Roel van der Zon was born in Borne, The Netherlands, in 1991. He received the B.Sc. degree in electrical engineering and the M.Sc. degree in electrical engineering, with a specialization in photonic integration from Eindhoven University of Technology (TU/e) in 2016 and 2019, respectively. He is currently pursuing the Ph.D. degree with UPVfab, Photonics Research Laboratories (PRL), Universitat Politècnica de València (UPV). During the master's thesis, he worked on hybrid strain and temperature measurements using fiber Bragg gratings and integrated lasers. At UPV the work is focused on the design and characterization of photonic integrated circuits. He is also involved in the fabrication processes developed with UPVfab.

Luis A. Bru received the B.Sc. degree in physics and the M.Sc. degree in advanced physics (specialty on photonics) from the Universitat de València (UV) in 2012 and 2013, respectively, and the Ph.D. degree from the Photonics Research Laboratories (PRL), Universitat Politècnica de València (UPV), in 2022. He is currently a Post-Doctoral Researcher with UPVfab, PRL, UPV, where he joined PRL in 2015. His research focused to advanced optical characterization of photonic integrated devices by employing interferometric techniques. This research has evolved toward wafer level testing development with UPVfab, activity he is currently in charge of. His research experience includes also quantum information diffusion modeling by quantum walks, having kept a research collaboration with nonlinear and quantum optics group with UV (2013–2017).

Daniel Pastor was born in Elda, Spain, in 1969. He received the Ph.D. degree in electrical engineering and telecommunications from the Universitat Politècnica de València, Spain, in 1996. His research career at photonics technologies started in 1993, where he joined the Optical Communication Group as a Researcher and the Communication Department, UPV, as a Lecturer. From 1994 to 1998, he was a Lecturer with the Telecommunications Engineering Faculty and he became an Associate Professor in 1999. His Ph.D. thesis topic "Redes de Difracción Sobre Fibra Óptica para Procesado de Señales Fotónicas." He is the coauthor of more than 225 papers in journals and international conferences in the fields of optical delay line filters, fiber Bragg gratings, microwave photonics, WDM and SCM lightwave systems, optical fiber sensors, silicon nitride integrated devices for telecom and sensing, and advanced characterization techniques as optical frequency domain reflectometry. His current research and technical interests include photonic integrated circuits for telecom, LiDAR and chemical, and bio-sensing applications.